ORBITAL MEASUREMENTS OF THE EARTH'S RADIATION BUDGET DURING

THE FIRST DECADE OF THE SPACE PROGRAM

William R. Bandeen
NASA Goddard Space Flight Center
Greenbelt, Maryland

INTRODUCTION

A knowledge of the radiation budget of the Earth-atmosphere system and its components (i.e., the total solar irradiance, its partition into absorbed and reflected shortwave radiation, and the infrared radiation emitted to space) is fundamental to an understanding of weather, climate, and possible climate change. During the period from 1959 to 1969, radiation budget studies were carried out using data from the Explorer 7, TIROS 2, 3, 4, and 7, and Nimbus 2 and 3 experimental satellites. Many difficulties were encountered in analyzing data from these early satellites, including the following:

The value of the solar "constant" was not accurately known

There was marked degradation of the sensors in orbit

The total reflected and emitted radiation had to be inferred from "filtered" measurements

Corrections for the anisotropy of the reflected and emitted radiances had to be developed to determine the outgoing flux densities at the moment of measurement

Corrections to account for diurnal variability had to be developed to estimate the daily average of outgoing flux densities (because of the "undersampled" nature of the data)

In spite of these sources of error, the early measurements indicated that the planetary albedo was lower (i.e., approximately 29 percent as opposed to 35 percent), the emitted radiation was higher, and the equator-to-pole gradient of net radiation was greater than had been previously supposed.

Lessons learned from these early satellites have been applied to later missions, and increasingly accurate determinations of the radiation budget are expected from the Earth Radiation Budget (ERB) sensors flown on Nimbus 6 and 7 and from the Earth Radiation Budget Satellite (ERBS) and NOAA F and G satellites scheduled for launch in 1984 and 1985.

EARTH-ATMOSPHERE HEAT ENGINE

Figure 1 illustrates the fact that the Earth-atmosphere heat engine is driven by the Sun. The incoming solar radiation, which amounts to about 173 000 TW, is either reflected or absorbed by the Earth-atmosphere system. The absorbed radiation is distributed either by surface heating or by latent heat transfer through water vapor condensation, with precipitation falling back to the surface of the Earth. A smaller amount is transferred to sensible heat. The potential energy available from differential heating of the atmosphere drives the winds, which in turn drive the ocean currents. Emitted longwave radiation is lost to space.

The albedo shown in figure 1, about 29 percent, is a value derived from measurements made during the first 10 years of space exploration. As an aside, it occurs to me that we have no energy problem on the planet Earth because all of mankind uses about 15 TW of energy, so that using only about 0.01 percent of the incoming solar radiation would enable us to meet our needs. Of course, the problem is learning how to tap that available energy.

EXPLORER 7 HEMISPHERICAL SENSORS

Explorer 7 was launched on October 13, 1959, about 21 years ago, and carried the wide-field-of-view hemispherical sensors developed by Verner Suomi. These sensors were mounted on aluminum mirrors, so they did not "see" the space-craft. They merely saw a reflection of the scene in the mirror, and thus acted virtually as spheres, radiatively isolated in space. The arrangement of the sensors on the spin-stabilized spacecraft is shown schematically in figure 2.

Equation (1) represents the radiation equation at night, when only infrared radiation is involved:

$$\alpha\beta W_L = 4\pi\varepsilon\sigma T^4 + 2H\frac{\partial T}{\partial t} + 2k(T - T_m) \tag{1}$$

where

$\alpha=\varepsilon$ infrared absorptivity, emissivity

β solid angle to Earth

σ Stefan-Boltzmann constant

T temperature of sensor

H heat capacity of sensor

t time

k   conductivity between sensor and mount (i.e., mirror
                 temperature, T_m)

W_L infrared radiant emittance of Earth

As shown on the right-hand side of the equation, the absorbed incoming longwave
radiation can produce three effects. First, it can be radiated back to space,
as expressed in the first term. Second, it can be stored in the mass of the
sensor by causing the sensor to heat at the rate shown. Third, it can cause
heat conduction from the sensor to the satellite or, in this case, to the
mirror. If the temperature of the mirror is less than the temperature of the
sensor, heat can be conducted to the mirror.

Results of analyzing the Explorer 7 radiation budget data are shown in fig-
ure 3. Isolines of nighttime radiation loss to space are shown superimposed on
surface positions of several weather fronts. It can be seen that the low of
outgoing radiation is associated with what must be cloud cover associated with a
low-pressure system. Measurements of surface fronts are synoptic, taken every
12 hours, while the satellite measurements are asynoptic, so it is difficult to
correlate the positions of the fronts with the radiation analysis when the
measurements are not necessarily taken at the same time. Moreover, wide-field
measurements like this will receive radiation from the entire disk of the Earth,
so when we say that a low occurs in a certain place it is really an integration
of measurements from the entire disk.

At its perigee of about 550 km, Explorer 7 saw out to a great circle arc of
about 25°. However, the majority of the measurements came from a rather
restricted area underneath the satellite. Despite the problems of rigorous
interpretation, this experiment showed the close relationship between outgoing
radiation and tropospheric weather patterns.

THE TIROS SERIES SCANNING RADIOMETERS

Vonder Haar (1968) analyzed many of the subsequent wide-field-of-view
measurements from experiments designed at the University of Wisconsin and con-
ducted with both hemispherical and flat-plate sensors flown on many of the early
TIROS satellites. A new radiation-sensing instrument, the five-channel scanning
radiometer, was flown on TIROS 2 (launched in November 1960), TIROS 3 (launched
in July 1961), and TIROS 4 (launched in February 1962). Each of the channels
had a rather narrow instantaneous field of view of about 5°; hence, the measure-
ments could be interpreted as being measurements of radiances rather than of
fluxes.

An attempt was made to analyze the radiation budget from these three
instruments on TIROS 2, 3, and 4, but there were difficulties. First, the
satellite had an inclination of only 48°, and therefore saw only a "quasi-globe,"
not the entire Earth. By quasi-globe we mean the region from 55°N to 55°S
latitude as viewed by the scanning radiometers. Shown in figure 4 is an example
of measurements of the quasi-global power interpreted in terms of the equivalent
albedo. The albedos interpreted from the early TIROS measurements were dis-
turbingly low, on the order of 15 to 17 percent. These values were about half

of what had been expected, even taking into account the following possible
sources of error:

Original calibration

Sensor degradation

Solar constant

Unfiltered radiation from filtered measurements

Angular dependence

Sampling problem

Calibration in the days of the TIROS satellites was a rather primitive
procedure, done without the benefit of specialized calibration facilities. The
calibration equation for the visible sensors was:

$$\bar{w}^* = \frac{\Omega}{\pi} \int_0^\infty w_\lambda \phi_\lambda \, d\lambda \tag{2}$$

where

$\bar{w}^*$ effective radiant emittance measured by sensor if it viewed a
perfectly diffuse, perfectly reflecting target (albedo = 1)
normal to incident solar radiation, $W\ m^{-2}$

Ω solid angle of Sun as seen from Earth

w_λ spectral radiant emittance of a 6000-K blackbody, $W\ m^{-2}\ \lambda^{-1}$

ϕ_λ spectral response function for channel

Solar spectral information available in those days led us to assume a solar
blackbody temperature of about 6000 K to fit the incident solar energy over the
bandwidth of the shortwave sensor, from about 0.2 to 5 µm.

In addition to such problems as possible calibration errors and a lack of
knowledge of the true solar constant and its spectral distribution, it was clear
that sensor degradation was a major problem on these early instruments. Another
form of wide-field low-resolution sensor, flown on TIROS 2 by Dr. Hanel of
Goddard Space Flight Center, degraded so quickly in just a few days of exposure
to space vacuum and solar ultraviolet and particle radiation that it was no
longer useable after a week of flight.

Apparent problems with sensors are indicated by the large difference
between the absorbed solar radiation (interpreted from quasi-global albedo) and
emitted terrestrial radiation obtained from the 8- to 12-µm and 8- to 30-µm
channels on TIROS 2, 3, and 4, as shown in figure 4. Obviously, if we are to
remain comfortable on the Earth, the emitted radiation in terms of quasi-global

power should approximately equal the absorbed solar radiation. If the differences indicated in figure 4 were real, the Earth should have been heating up so fast that we should have been boiling after a few months.

Note that in every case the longwave value observed at launch decreased with time. We already had a qualitative idea of how longwave and reflected radiation should behave, based on the earlier work of Dr. London and others (London, 1957). The observed behavior was so persistent and regular, and so consistently out of agreement with what we expected, that it was interpreted as being due to sensor degradation in space rather than to a real phenomenon. Since the science of materials in the space environment was not very far advanced at the time of the TIROS satellites, a likely cause of sensor degradation was the use of unsuitable materials for coating the sensor surfaces. It is reasonable to assume that the black paints used on the chopper of the sensor boiled off of one side and coated the other, mirrored, side.

TIROS 7 MEASUREMENTS

The first satellite to provide a continuous record for 1 year was TIROS 7, launched in June 1963. It used the same instrument as was flown on TIROS 2, 3, and 4. In figure 5, effective radiant emittance as measured from TIROS 7 is plotted versus time for 1 year from June 1963 to June 1964. We looked first at measurements over the equatorial Pacific Ocean, where we expected the seasonal variations to be small between about 30°N and 30°S latitude. However, the measurements again showed clear evidence of degradation of the instrument with time. We also looked at the so-called quasi-global map averages and again found evidence of degradation.

The sinusoidal curve at the top of each part of figure 5 is an attempt to take into account the changing geometry between the Sun and the satellite orbit plane. The inclination of TIROS 7 was 58°, and the precession of this orbit plane relative to the Sun has a period of about 76 days. Looking from the Sun, one would see the descending node on the longitude of the subsolar point shortly after launch. The orbit regresses to the west, and after about 20 days the orbital plane as viewed from the Sun would shift as shown in figure 6. The different orbital geometries noted in figure 6 correspond to the numbered points on the orbit-Sun-phase sinusoidal curve at the top of figures 5(a) and (b).

Because of the changing orientation of the orbit plane relative to the Sun, we expected substantial differences when analyzing the quasi-globe if we were looking, say, at the Northern Hemisphere in summer in the sunlight and the Southern Hemisphere in winter at night. We grouped these orbit plane configurations into regimes, took approximately 2-week averages in each regime, and averaged them to try to smooth out the diurnal variations that we suspected in a given latitude band. However, we still found a marked degradation of the infrared channel and, similarly, an apparent degradation in the reflectances through the visible channel. Therefore, in analyzing these data we had to develop an empirical time correction factor which simply extrapolated each point back to the time of launch.

TIROS 7 had two other channels which would have been better for radiation budget analyses. One was a broad infrared channel covering wavelengths from 5 to 30 μm, but this channel exhibited greater degradation than the narrower 8- to 12-μm channel. We had to develop a regression equation to try to convert the severely filtered 8- to 12-μm radiance to an equivalent total outgoing unfiltered radiance. Similarly, there was a 0.2- to 5-μm channel that would have been much better for making reflectance measurements, but it degraded much more severely than the 0.55- to 0.75-μm channel. Therefore, we had to infer albedo from the narrower, severely filtered channels even though we would have preferred to use the broader channels.

After making some rather simplistic corrections for obvious degradation, we obtained curves of longwave radiation zonally averaged from 90°S to 90°N, which we compared to London's (1957) Northern Hemisphere results. This comparison is shown in figure 7(a). We could not attach much significance to the fact that our outgoing longwave radiation was a little greater than London's, because our data had been subject to so many corrections.

In figure 7(b) we have plotted our inferred albedo compared to London's (1957) data. Here we could be even less confident of our values, because even after making our so-called corrections for degradation from launch we found that we had to multiply the resultant albedos by a factor of 1.6 in order to create radiative equilibrium over the quasi-globe. (Even our requirement that the quasi-globe must be in equilibrium is an assumption.) We finally determined that the quasi-global albedo was 32.2 percent. We had some indication that the outgoing longwave radiation might have been a little greater than London's analysis and the albedo might have been a little lower. In fact, the indications were that the albedo was quite a bit lower in the tropics and somewhat higher in the high latitudes. This would indicate that the "firebox" in the atmospheric engine was hotter than was previously supposed, which in turn would demand that the equatorial transport of heat to higher latitudes was greater than had been supposed.

THE NIMBUS SATELLITE SERIES

The Medium-Resolution Infrared Radiometer (MRIR) was a five-channel instrument flown on the Nimbus satellites. MRIR is actually a misnomer since one of the channels was a visible channel which monitored radiation from the Sun between 0.2 and 5.0 μm. The other four channels, however, did respond to various parts of the infrared spectrum. The IFOV of each channel was a little less (about 2.8°) than those on the TIROS instrument.

A four-step sequence was devised to analyze the MRIR data from Nimbus 2 and 3, the two satellites on which the MRIR was flown. First, the total shortwave and longwave unfiltered radiances had to be computed from filtered radiances. (This computation is one of the possible sources of error mentioned previously.) Next we had to correct for the anisotropy, or angular dependence, of the radiances for the limb darkening in the case of infrared radiances, and the anisotropy of backscattered solar radiation through clouds, oceans, land, etc. Statistical models had to be used, since the satellite flew over at 7 km/sec and a given spot on the Earth was therefore viewed at only one angle.

We had to infer the radiances at all angles over the upper hemisphere from that spot, even though only one measurement was made at a given set of zenith and azimuth angles.

The third step involved an integration over all angles to obtain the outgoing flux density at the moment of measurement. Here one could use only a finite number of practical situations in the ranges of solar zenith angle in order to make this a tractable problem. Finally, we had to compute the daily averages of outgoing flux, both reflected solar radiation and infrared emitted radiation, having made a determination of this flux only at the instant the satellite flew over. This brings forward the familiar sampling problem. Nimbus was in a noon-midnight Sun-synchronous orbit, so that measurements were made only at noon and midnight, local time, at low latitudes. The angular convention used in the analyses of infrared data from Nimbus 2 and 3 is shown in figure 8.

Nimbus 2 and 3

Nimbus 2 was launched on May 15, 1966, and Nimbus 3 on April 14, 1969. Nimbus 2 had a broad infrared channel, from about 5 to 30 μm, which would have been better than a number of narrow channels in the infrared part of the spectrum for radiation budget measurements. Unfortunately, the Nimbus 2 MRIR lasted only 2-1/2 months. It was launched in May and it became inoperative at the end of July. We did, however, carry out analyses of the data and publish results (Raschke and Bandeen, 1970).

Nimbus 3 provided measurements over an entire year, and we consider those measurements to be more significant than those of Nimbus 2, which were made over only 10 weeks. Unfortunately for radiative budget purposes, the MRIR on Nimbus 3 was modified to have four rather narrow spectral channels in the infrared: one around the water vapor absorption band at 6.7 μm, one around the window at between 10 and 12 μm, one around the CO_2 absorption band at 15 μm, and one at the rotation water vapor absorption region around 20 μm. (See fig. 9.)

To calculate values for longwave outgoing radiation in the infrared, we first had to develop a regression equation to compute the total radiance in the direction of the satellite using filtered measurements made in four different channels, as described previously:

$$N_t = a_0 + a_1 N_2 + a_2 N_2^2 + a_3 N_2^3 + a_4 N_4 + a_5 N_1 + a_6 N_3 \tag{3}$$

where

a   regression coefficients

N   radiances measured at channels shown in figure 9

We calculated three coefficients for channel 2 (the window channel) and only one for the other three channels. The 10- to 12-µm channel (the window channel) had a much more significant effect than the other channels, and this is reflected in the equation by including a set of higher order terms for this channel. Since the other three channels had a much smaller effect on the total radiation, only first-order terms were used.

To develop the coefficients here we used the early work of Wark et al. (1962), which used 105 model atmospheres in a computer program that served many purposes in the first 10 years and beyond in the space program. Having used that program to develop the regression coefficients, we now had a means of developing the total radiance across the entire spectrum in the direction of the satellite.

Correction for Longwave Anisotropy

The next step is to correct for the anisotropy of the longwave radiation by integrating over all angles to obtain the total outgoing longwave flux density at the moment of measurement. The total longwave radiant emittance is the integral of the total radiance in the direction θ over all data from the zenith down to the horizon, over all azimuth angles:

$$W_L = \int_0^{2\pi} \int_0^{\pi/2} N_t(\theta) \sin\theta \cos\theta \, d\theta \, d\psi \qquad (4)$$

where

N_t total radiance in direction θ

W_L total longwave radiant emittance

θ zenith angle of radiance

ψ azimuth angle of radiance

Since the radiance is assumed not to be a function of azimuth, the 2π can be taken out of the integral. Further, we can develop a limb-darkening model which relates the radiance that would be observed at nadir to a radiance measurement in an arbitrary direction. Then we are left only with an integral over a limb-darkening function $f(\theta)$:

$$W_L = 2\pi N_t(\theta=0^\circ) \int_0^{\pi/2} f(\theta) \sin\theta \cos\theta \, d\theta \qquad (5)$$

This limb-darkening function would be the radiance over the total spectrum in the direction θ divided by the radiance in the zenith direction. We approximated this ratio by using measurements from the Nimbus 2 broadband

instrument (5 to 30 µm). Even though Nimbus 2 only lasted 10 weeks, we had a good sample of data from which to take the ratio of the radiance in the broad infrared channel at various angles θ to the radiance in the zenith direction. This enabled us to develop an expression for the limb-darkening corrections:

$$f(\theta) = \frac{N_t(\theta)}{N_t(\theta=0^\circ)} \approx \frac{N_{5-30\ \mu m}(\theta)}{N_{5-30\ \mu m}(\theta=0^\circ)} = 1 + b_1\theta + b_2\theta^2 + b_3\theta^3 \tag{6}$$

where

  b   regression coefficients

Having developed the limb-darkening models, we could integrate and determine the total outgoing longwave radiation in the upper hemisphere at the instant of measurement.

The limb-darkening functions were developed for five cases; two extremes are shown in figure 10. The function varies from less than 0.8 to 1.0 for the entire range of zenith angles between 0° and 90°. The function is, by definition, equal to 1 at a zenith angle of 0°. The arctic function was the least severe, and the desert curve was the most severe. An antarctic curve falls just under the arctic curve. Midlatitude and tropical curves are nearly identical, and fall between these two extremes.

This still left the problem of computing daily averages. Since we could not know what happened to the outgoing radiation between the instant the satellite passed over at noon and the instant around midnight when it happened to pass over the same place, we simply averaged the noon and night measurements with equal weighting and assumed that this was somehow representative of the diurnal variability.

Correction for Shortwave Anisotropy

The total unfiltered radiances are computed by assuming that the bidirectional reflectance behavior over the total spectrum is the same as the behavior inferred in the 0.2- to 4-µm band. This is a rather broad band and contains virtually all of the solar radiation. The bidirectional reflectance function ρ is defined as the ratio of measured radiance reaching the satellite at a zenith angle θ and azimuth angle ψ with a solar zenith angle ζ, at a time t', to the incoming filtered distance-corrected solar constant S_f at the same solar zenith angle and time:

$$\rho(\theta,\psi,\zeta;t') = \frac{N_f(\theta,\psi,\zeta;t')}{S_f L \cos \zeta(t')} \tag{7}$$

where

N_f filtered radiance

t' measurement time

L   ratio squared of mean to true Earth-Sun distance

Now we can integrate over all angles to obtain the outgoing flux density at the time of measurement. We want to determine the directional reflectance r, i.e., the radiation reflected over the entire upper hemisphere divided by the solar radiation incident on the target at that same time. This would be the integral of the bidirectional reflectance over the upper hemisphere:

$$r(\zeta;t') = \int_0^{2\pi} \int_0^{\pi/2} \rho(\theta,\psi,\zeta;t') \sin\theta \cos\theta \, d\theta \, d\psi \qquad (8)$$

However, the bidirectional reflectance was measured at only one satellite and solar zenith angle at one instant in time before the satellite moved on to another place. Since the satellite could not hover and look at all angles over the upper hemisphere, we had to develop a model to infer the total reflectance at all angles in the upper hemisphere based on measurements from one particular direction. We developed a function χ which was multiplied by the measured bidirectional reflectance at a given angle θ and ψ, solar zenith angle ζ, and time of measurement t', and then multiplied this by π. The departure from anisotropy is reflected in this function χ:

$$r(\zeta;t') = \chi(\theta\psi\zeta) \, \pi\rho(\theta,\psi,\zeta;t') \qquad (9)$$

where

r   directional reflectance

χ directional reflectance function

and

$$\chi(\theta,\psi,\zeta=\text{const.}) = \frac{r(\zeta=\text{const.})}{\pi\rho(\theta,\psi,\zeta=\text{const.})} \qquad (10)$$

Figure 11 is an example of the kind of bidirectional reflectance functions we developed. We used only three ranges of solar zenith angles to keep the problem tractable. The figure shows the models for solar zenith angles between 35° and 60° and between 60° and 80°. We developed another model for the range between 0° and 35°. Models like this were developed for three different surface types: (1) an ocean clear-sky model, defined as a situation in which the directional reflectances were 0.1 or less and the observed surface temperature

was greater than or equal to 273 K so that the surface was not frozen; (2) a snow model for use whenever the directional reflectance was greater than 0.5 and the latitude was greater than 65°; and (3) a "land" model for all other cases. In summary, we produced a total of nine different models similar to those shown in figure 11.

The left side of figure 11 illustrates a situation in which the Sun is at a large zenith angle, around 70°. If the satellite looks back to see the radiation in the direction from which the Sun is shining, we would expect to see a strong forward scattering. If we assumed a Lambertian surface to infer the total flux from a beam measurement made in a region of strong forward scattering, then we would overestimate the total scattering. We would consequently expect the χ function to be less than 1 in other directions, so that when the bidirectional reflectance in a region of strong forward scattering is multiplied by the χ function this would give the proper directional reflectance over the whole upper hemisphere. Indeed, it can be seen that χ is 0.9 at a satellite zenith angle of 50°. If more data were available, we would find χ values even as low as 0.5 at larger θ angles.

The data for developing the χ functions came from several different sources. Shown in figure 12 are bidirectional reflectance models developed from a series of measurements made from the NASA Convair 990 aircraft stationed at Ames Research Center. An engineering model of the MRIR was mounted in the tail of this aircraft and flown over a variety of targets using several flight patterns to try to obtain a representative number of viewing zenith and azimuth angles for measuring scattered radiation. Flights were made at different times of the day to make measurements over a range of solar zenith angles. Figures 12(a) and (b) show the resulting bidirectional models obtained from flights over the Pacific Ocean at an altitude of 40,000 ft and an azimuth angle of 0° (looking back at the Sun), and are illustrative of the rather strong forward scattering that occurs over the uniform stratocumulus clouds encountered there. The bidirectional reflectances vary from about 7 percent at nadir to about 45 percent near the horizon. The derived directional models are shown in figure 12(c). Models like these are representative of those made using data from the Convair 990 and other sources in this country and Europe, as well as from analyses of the early TIROS data (Arking, 1965; Arking and Levine, 1967).

Having determined directional reflectance at the instant of measurement, we still have to infer the reflectance over the entire day from sunrise to sunset in order to compute daily averages of reflected and absorbed solar radiation. The total outgoing radiation for a solar day (1440 minutes) integrated from sunrise to sunset is:

$$R = \frac{1}{1440} \int_{t_r}^{t_s} SL \cos \zeta(t) \ r[\zeta(t)] \ dt \tag{11}$$

where

S   solar spectral radiance

t_s, t_r times of sunset and sunrise, respectively

R   total outgoing radiation for 1 day

To evaluate this integral we developed a function E which was defined as the directional reflectance (a function only of solar zenith angle for any given target) divided by the directional reflectance for that target at a solar zenith angle of 0°. The three directional reflectance models used on Nimbus 3 are shown in figure 13. The ocean model shows strong forward scattering as the Sun approaches either sunset or sunrise, the snow model (Kondratiev et al., 1968) shows little dependence on zenith angle, and the cloud-land model lies in between. For comparison, the single Nimbus 2 model is also shown; this was applied to all surface types (Raschke and Bandeen, 1970; Raschke et al., 1973a, b). The flatness of the snow model is due to the fact that the strong forward scattering is balanced by very weak backscattering, so that an integration over the hemisphere yields a very flat curve for the directional (as opposed to the bidirectional) model. Now equation (11) becomes:

$$R = \frac{1}{1440} \int_{t_r}^{t_s} SL \, \cos \, \zeta(t) \, \frac{r(\zeta;t')}{E(t')} \, E(t) \, dt \qquad (12)$$

where

E   the function $r[\zeta(t)]/r(\zeta=0^\circ)$

Analysis of Nimbus 3 data yields results such as those shown in figure 14. The albedo was found to be about 28.4 percent and the longwave emission was about 0.345 cal cm^{-2} min^{-1}. Some areas exhibit radiation surpluses, defined as more absorbed solar radiation than outgoing longwave radiation, and others exhibit deficits, defined as more outgoing longwave radiation than absorbed solar. This lack of balance is what drives the atmospheric heat engine.

A significant feature is the deficit found over the Sahara Desert. This deficit has been interpreted as an annual feature based on our measurements from May 1969 to February 1970. The results surprised many people because it was assumed that there should be a surplus of radiative energy, as defined, over that hot low-latitude desert. At about the same time Jule Charney was developing some theoretical models which, surprisingly, predicted the same sort of radiation deficit over hot deserts at low latitude. The satellite data shown in figure 14 confirmed his predictions, which can be explained qualitatively by noting that the high desert albedo prevents absorption of enough radiation to produce a surplus.

The Nimbus satellites were in a Sun-synchronous orbit (fig. 15), as are the NOAA operational satellites today. The inclination of the orbit plane is 98.6°. The oblateness of the Earth makes the orbital plane regress at a rate

of 0.9856° per day, the same rate as the average apparent motion of the Sun around the celestial sphere. Hence, the Nimbus satellites always cross the equator at the same local time. In the case of Nimbus, it is noon (local time) when the satellite crosses the equator from south to north, and midnight on the other side of the Earth when the satellite crosses the equator from north to south. This caused severe problems for our method of determining the outgoing radiation over all hours of the day; we had no way of knowing the diurnal variability for Nimbus. Therefore we just assumed that the target conditions viewed at noon persisted from sunrise to sunset. The meteorology was actually hardly ever constant in this way, but we simply did not know what else to do.

The early TIROS spacecraft had non-Sun-synchronous orbits, as does one of the proposed ERBE satellites. In this case the orbit plane precesses relative to the Sun such that all available latitudes can eventually be sampled at all local times, typically over about a 2-month period. Vonder Haar (1968) made a study of diurnal variability from the early TIROS satellites. He demonstrated that the minimum albedo occurred at around 9:00 or 10:00 a.m. and the maximum at around 2:00 or 3:00 p.m. These positions are reversed for infrared radiation. His results are shown in figure 16. At the times of minimum albedo there is maximum infrared radiation loss. When the albedo is high, as in cloudy scenes, there is a minimum of infrared radiation loss to space. We found that the Nimbus results fell somewhere in between these peaks and gave an overall balance. Results from the ERBE measurements will tell in a few years how good or bad the Nimbus results were.

HISTORICAL DETERMINATIONS OF SOLAR CONSTANT AND ALBEDO

The solar "constant" is a source of error in all these radiation calculations. Values for the solar constant which have been determined over the last 57 years are given in table I, beginning with Abbott's early measurements made at the Smithsonian Institution over a 30-year period (Abbott, 1922). His value was 1352 W m^{-2}, or 1.94 ly min^{-1}. Johnson (1954) obtained a slightly higher value of 1395 W m^{-2}, or 2.0 ly min^{-1}; this was the solar constant used in the TIROS and Nimbus 2 analyses. Verner Suomi and his colleagues at the University of Wisconsin made a determination of the solar constant from analyses of wide-field-of-view satellite measurements (Vonder Haar, 1968). These early experiments were useful because they were extremely simple. Using the complete form of equation (1), which includes solar radiation terms, the variation of sensor heating with time could be used to determine several things, such as the solar constant.

In 1966 Drummond and coworkers determined the value of the solar constant at 1360 W m^{-2} (Drummond et al., 1967). Willson and coworkers determined the value at 1368 W m^{-2} in June 1976 and 1373 W m^{-2} in November 1978 (Willson et al., 1980). The 1978 value represents about a 0.4-percent increase over their first value. Willson et al. state that this might be the true indication of the variability of the solar constant.

A rocket flown in May 1980, at the peak of the solar cycle, gave the same value as that determined in November 1978. Hickey et al. (1980) recently published a result of the Nimbus 7 ERB cavity radiometer (1376 W m^{-2}), and

Willson's latest value, taken from the Solar Maximum Mission launched on February 14, 1980, is 1368 W m^{-2} (Willson et al., 1981). Many researchers are concluding that these changing values reflect the fact that there is actually some variability in the solar constant.

The Solar Maximum Mission value of 1368 W m^{-2} has shown a variation of a few tenths of a percent over short time intervals. Instrument calibration and degradation are two possible sources of error mentioned earlier which are of concern in this mission when trying to make very precise measurements. For instance, Willson compared measurements made with two instruments both on the ground and in rocket flights and found unexplained variations which make the small percentage changes found in data from the Solar Maximum Mission more suspect (Willson et al., 1980; R. C. Willson, private communication).

Values of the Earth albedo determined by various researchers over the past 63 years are given in table II. There is an amazing, almost monotonic, decrease in these measurements over the years, again reflecting the introduction of more sophisticated instruments and improved methods of data analysis.

REFERENCES

Abbott, C. G.   1922:   Application of Solar Radiation Measurements.   Annals of
   the Astrophysical Laboratory of the Smithsonian Institution - IV, Chapter 6,
   The Smithsonian Institution, Washington, D.C.

Aldrich, L. B.   1919:   The Reflecting Power of Clouds.   Smithsonian Misc. Coll.,
   vol. 69, no. 10, pp. 1-9.

Angstrom, Anders   1962:   Atmospheric Turbidity, Global Illumination, and
   Planetary Albedo of the Earth.   Tellus, vol. 14, no. 4, pp. 435-450.

Arking, A.   1965:   The Angular Distribution of Scattered Solar Radiation and
   the Earth Albedo as Observed From TIROS.   Annual Research Report, Goddard AFC,
   July 1964-June 1965, pp. 47-67.

Arking, A.; and Levine, J. S.   1967:   Earth Albedo Measurements: July 1963 to
   June 1964.   J. Atmos. Sci., vol. 24, no. 6, pp. 721-724.

Bandeen, W. R.; Halev, M.; and Strange, I.   1965:   A Radiation Climatology in
   the Visible and Infrared From the TIROS Meteorological Satellites.   NASA
   TN D-2534.

Baur, F.; and Phillipps, H.   1934:   Der Warmehaushalt der Lufthulle der
   Nordhalbkugel in Januar and Juli und zur Zeit der Aquinoktien und Solstitien.
   Part 1.   Die Einstrahlung bei normaler Solarkonstante.   Gerlands Beitr.
   Geophys., vol. 42, pp. 160-207.

Dines, W. H.   1917:   The Heat Balance of the Atmosphere.   Quart. J. Roy.
   Meteorol. Soc., vol. 43, no. 182, pp. 151-158.

Drummond, A. J.; Hickey, J. R.; Scholes, W. J.; and Love, E. G.   1967:   Multi-
   channel Radiometer Measurement of Solar Irradiance.   J. Spacecr. & Rockets,
   vol. 4, no. 9, pp. 1200-1206.

Fritz, S.   1949:   The Albedo of the Planet Earth and of Clouds.   J. Meteorol.,
   vol. 6, no. 4, pp. 277-282.

Hickey, J. R.; Stowe, L. L.; Jacobowitz, H.; Pellogrino, P.; Maschhoff, R. H.;
   House, F.; and Vonder Haar, T. H.   1980:   Initial Solar Irradiance Determina-
   tions From Nimbus 7 Cavity Radiometer Measurements.   Science, vol. 208,
   no. 4441, pp. 281-283.

Houghton, H. G.   1954:   On the Annual Heat Balance of the Northern Hemisphere.
   J. Meteorol., vol. 11, no. 1, pp. 3-9.

House, Fred B.   1965:   The Radiation Balance of the Earth From a Satellite.
   Ph. D. Thesis, Univ. of Wisconsin, Madison.   (Available as NASA CR-76422.)

Johnson, F. S.   1954:   The Solar Constant.   J. Meteorol., vol. 11, no. 4,
   pp. 431-439.

Kondratiev, K. Ya.; Dyachenko, L. N.; and Vinnikov, K. Ya. 1968: The Climatology of the Net Radiation of the Earth. Paper presented at Symposium on Radiation, Including Satellite Techniques (Bergen, Norway), August 22-28.

Lettau, H. 1954: A Study of the Mass, Momentum, and Energy Budget of the Atmosphere. Archiv. Meteorol. Geophys. Bioklim. A, vol. 7, no. 1, pp. 133-157.

London, Julius 1957: A Study of the Atmospheric Heat Balance. AFCRC-TR-57-287, ASTIA no. 117227, Coll. Eng., New York Univ., July.

National Aeronautics and Space Administration 1961: Juno II Summary Project Report. Vol. I, Explorer VII Satellite. NASA TN D-608.

National Aeronautics and Space Administration 1963: TIROS 4 Radiation Data Catalog and Users' Manual. NASA TM X-72526.

Raschke, E.; and Bandeen, W. R. 1970: The Radiation Balance of the Planet Earth From Radiation Measurements of the Satellite Nimbus II. J. Appl. Meteorol., vol. 9, no. 2, pp. 215-238.

Raschke, E.; and Pasternak, M. 1968: The Global Radiation Balance of the Earth Atmosphere System Obtained From Radiation Data of the Meteorological Satellite Nimbus II. Space Research, VIII, North Holland Publ. Co., Amsterdam.

Raschke, Ehrhard; Vonder Haar, Thomas H.; Bandeen, William R.; and Pasternak, Musa 1973a: The Annual Radiation Balance of the Earth-Atmosphere System During 1969-70 From Nimbus 3 Measurements. J. Atmos. Sci., vol. 30, no. 3, pp. 341-364.

Raschke, Ehrhard; Vonder Haar, Thomas H.; Pasternak, Musa; and Bandeen, William R. 1973b: The Radiation Balance of the Earth-Atmosphere System From Nimbus 3 Radiation Measurements. NASA TN D-7249.

Simpson, G. C. 1928: Further Studies in Terrestrial Radiation. Mem. Roy. Meteorol. Soc., vol. 3, no. 21, pp. 1-26.

Vonder Haar, Thomas H. 1968: Variations of the Earth's Radiation Budget. Ph. D. Thesis, Univ. of Wisconsin, Madison.

Wark, D. Q.; Yamamoto, G.; and Leinesch, J. H. 1962: Methods of Estimating Infrared Flux and Surface Temperatures From Meteorological Satellites. J. Atmos. Sci., vol. 19, no. 5, pp. 369-384.

Willson, R. C.; Duncan, C. H.; and Geist, J. 1980: Direct Measurement of Solar Luminosity Variation. Science, vol. 207, no. 11, pp. 177-179.

Willson, R. C.; Gulkis, S.; Janssen, M.; Hudson, H. S.; and Chapman, G. A. 1981: Observations of Solar Irradiance Variability. Science, vol. 211, no. 4483, pp. 701-702.

TABLE I.- MEASUREMENTS OF SOLAR CONSTANT

Reference	W m^{-2}	ly min^{-1}
Abbott (1922)	1352	1.94
Johnson (1954)	1395	2.00
Vonder Haar (1968) (wide-field satellite sensors)	1388	1.99
Drummond et al. (1967) (aircraft)	1360	1.95
Willson et al. (1980)		
June 1976	1368	1.96
November 1978	1373	1.97
Hickey et al. (1980) (Nimbus 7 ERB)	1376	1.97
Willson et al. (1981) (Solar Maximum Mission)	1368	1.96

TABLE II.- EVOLUTION OF PLANETARY ALBEDO

Reference	Albedo, percent
Dines (1917)	50
Aldrich (1919)	43
Simpson (1928)	43
Baur and Phillipps (1934)	41.5
Fritz (1949)	34.7
Houghton (1954)	34
Lettau (1954)	34
London (1957)	35
Angstrom (1962)	33-38
House (1965)	35
Bandeen et al. (1965) (TIROS 7)	32
Raschke and Pasternak (1968) (Nimbus 2)	30
Vonder Haar (1968)	29
Raschke et al. (1973a, b) (Nimbus 3)	28.4
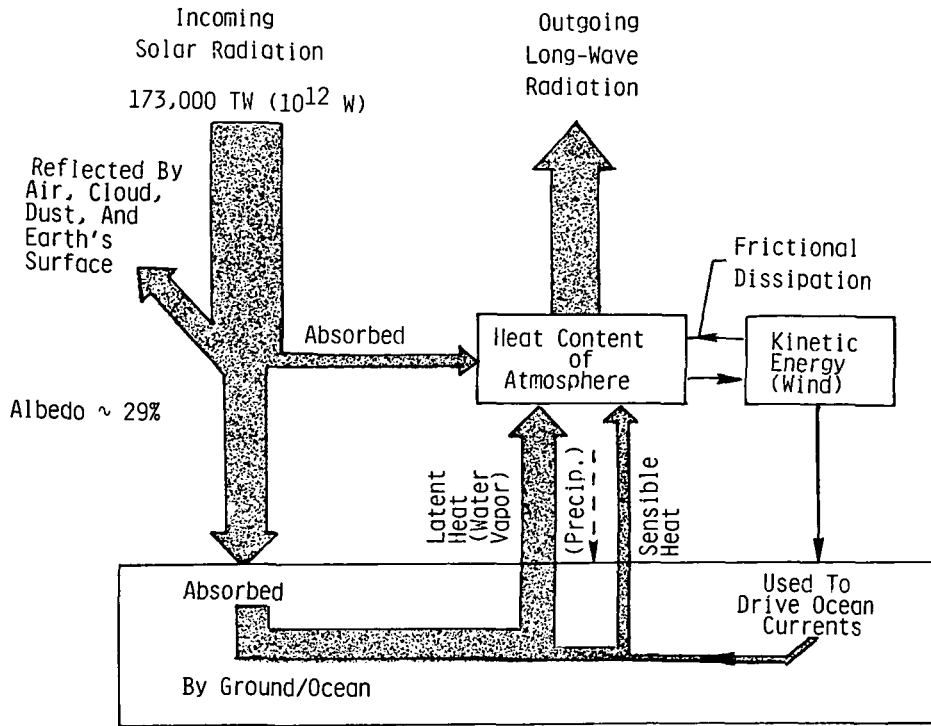
Figure 1.- Earth-atmosphere heat engine.
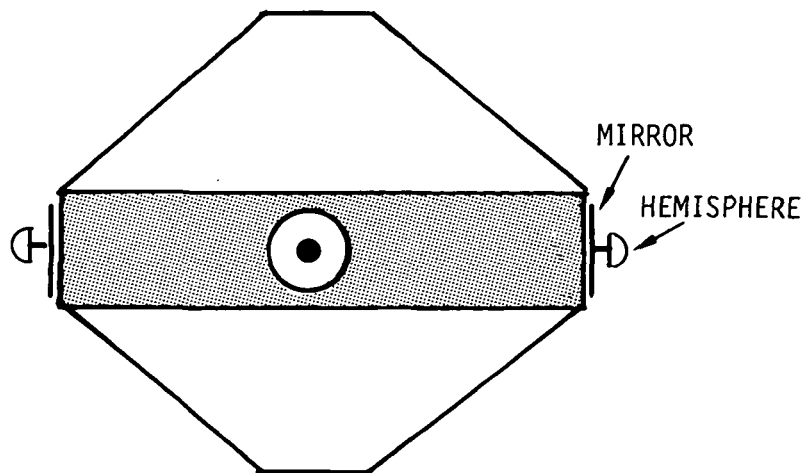
Figure 2.- Explorer 7 satellite hemispherical sensors.
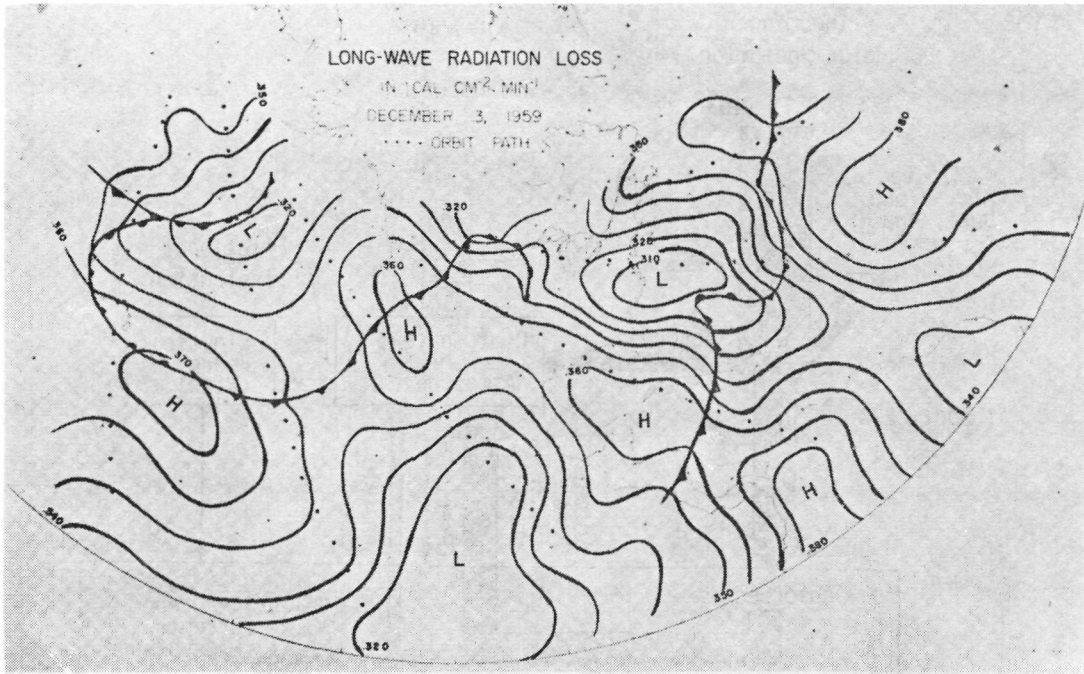
Figure 3.- Explorer 7 thermal radiation balance experiment.
(From National Aeronautics and Space Administration, 1961.)
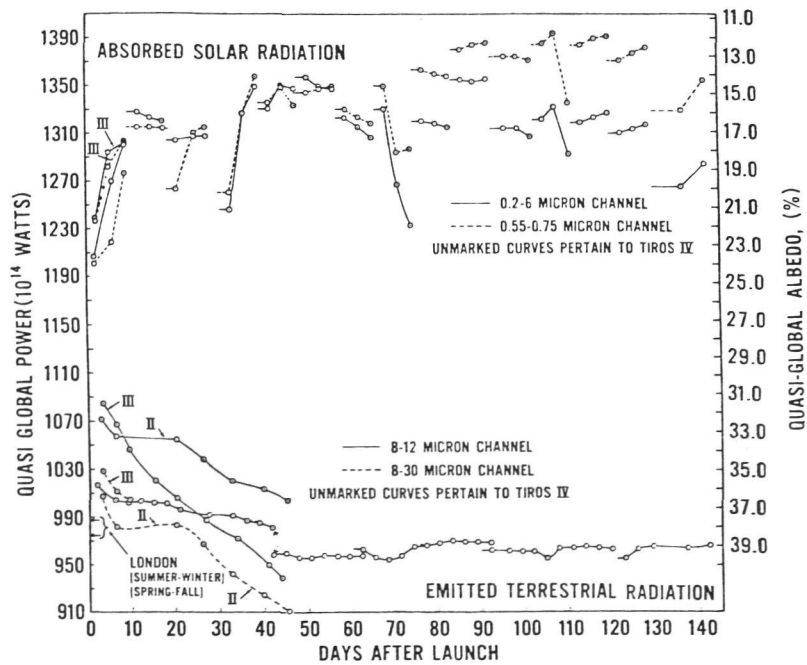
Figure 4.- Quasi-global (55°N to 55°S) radiative energy budget
as inferred from TIROS 2, 3, and 4 measurements. (From
National Aeronautics and Space Administration, 1963.)

20
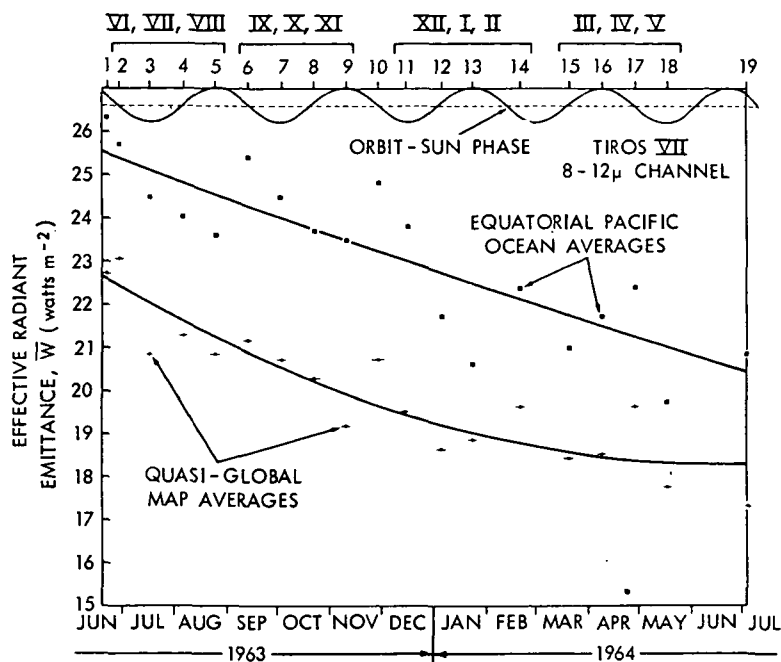
(a) Emitted radiation.
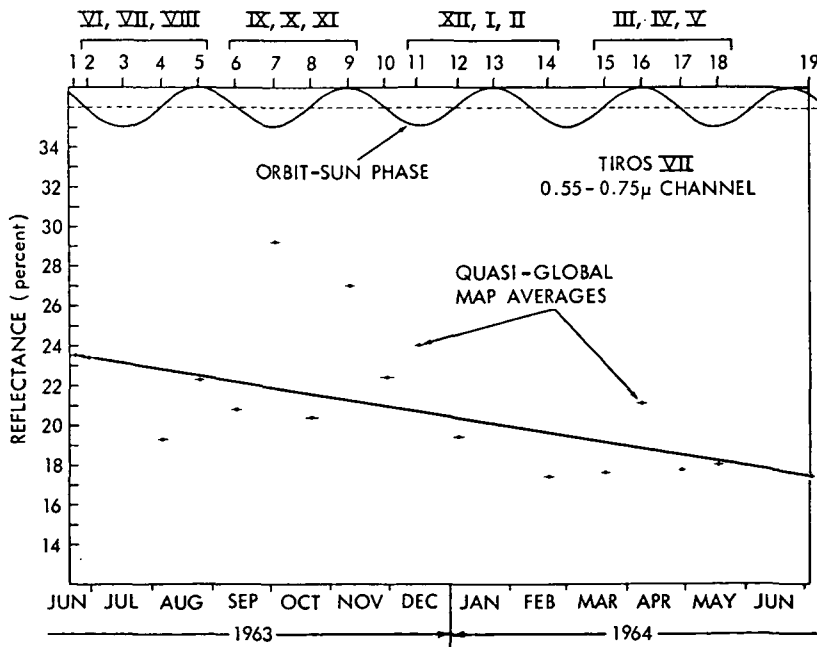
(b) Reflected radiation.

Figure 5.- Radiation measurements from TIROS 7.
(From Bandeen et al., 1965.)

POINT 2, 6   POINT 3   POINT 4   POINT 5
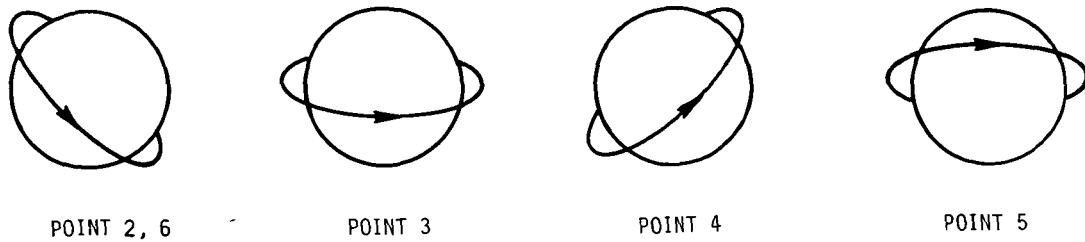
Figure 6.- Satellite orbit geometries correlated with numbered
points on sinusoidal curve at top of figures 5(a) and (b).
Synodic period is 76 days.

(a) Longwave radiation.   (b) Albedo.
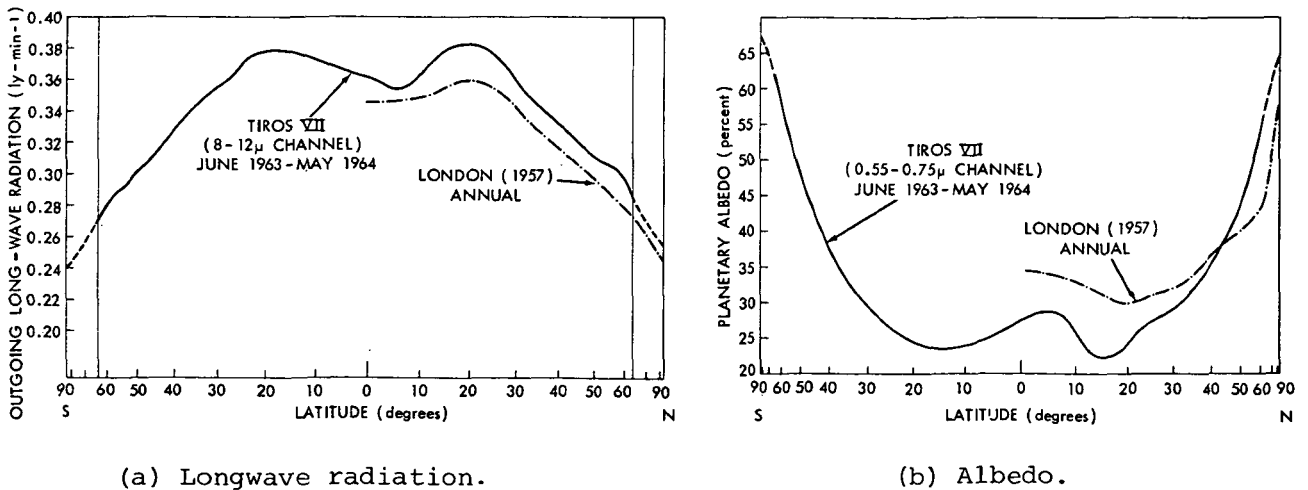
Figure 7.- Annual mean albedo and outgoing longwave radiation.
(Note: albedo above 55 percent was extrapolated using the
slope obtained from London's (1957) Northern Hemisphere
analysis.) (From Bandeen et al., 1965.)
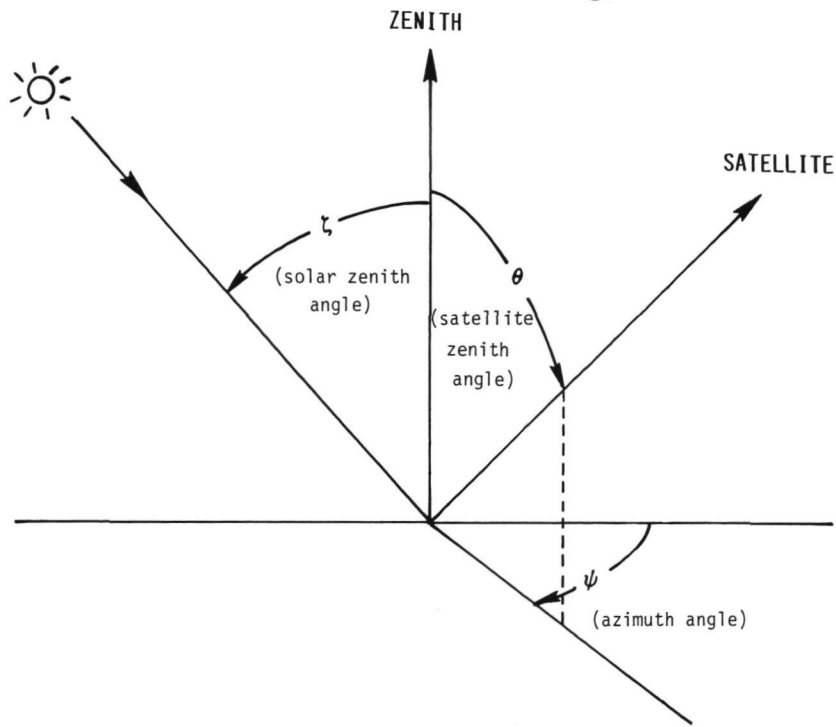
Figure 8.- Angular convention used in analyzing MRIR data from Nimbus 2
(launched May 15, 1966) and Nimbus 3 (launched April 14, 1969).
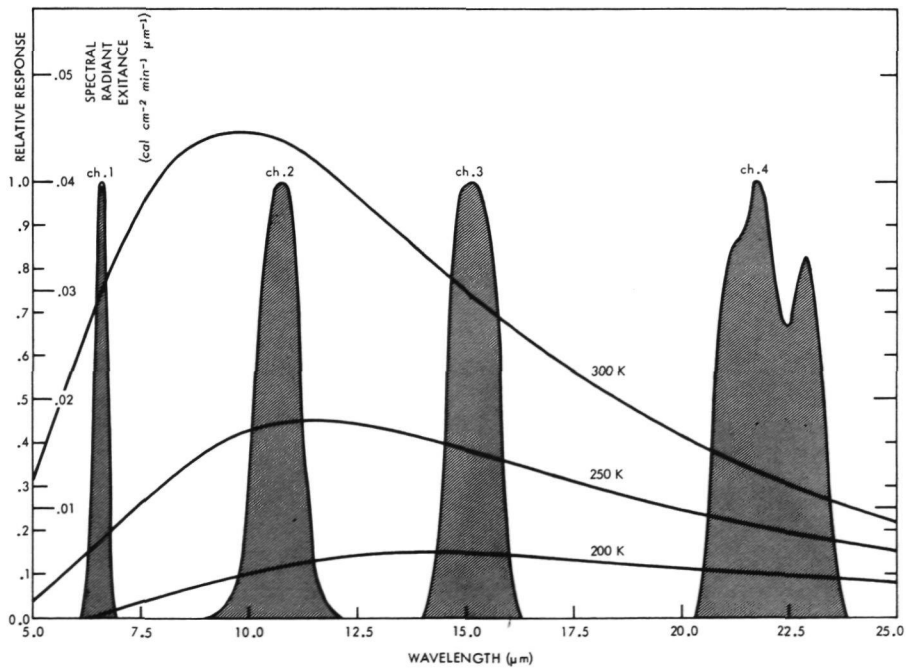
Figure 9.- Approximate spectral sensitivity of four channels on modified
MRIR and spectral radiant exitance of a blackbody at temperatures of
200, 250, and 300 K.   (From Raschke et al., 1973.)
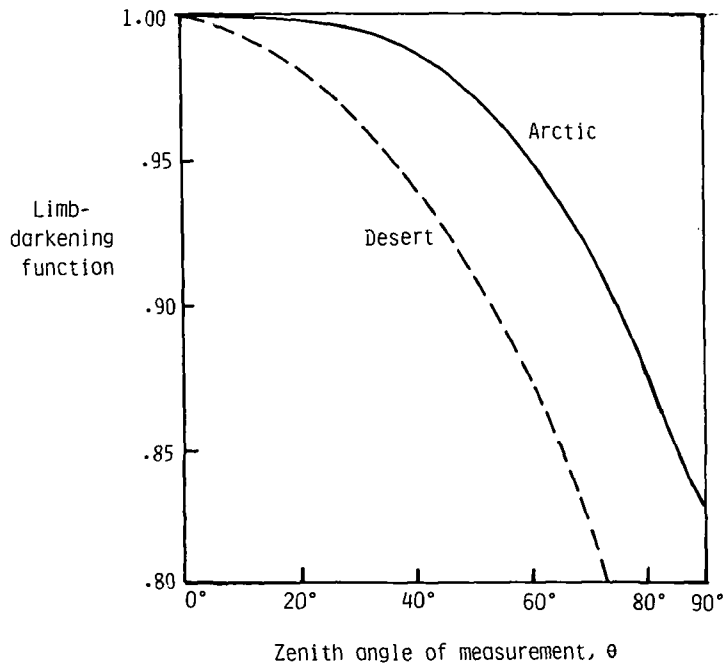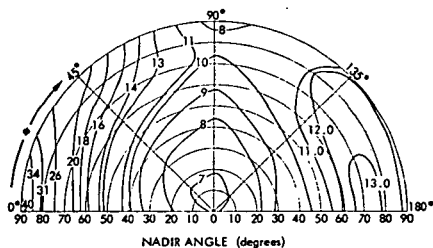
Figure 10.- Longwave radiation limb-darkening function.
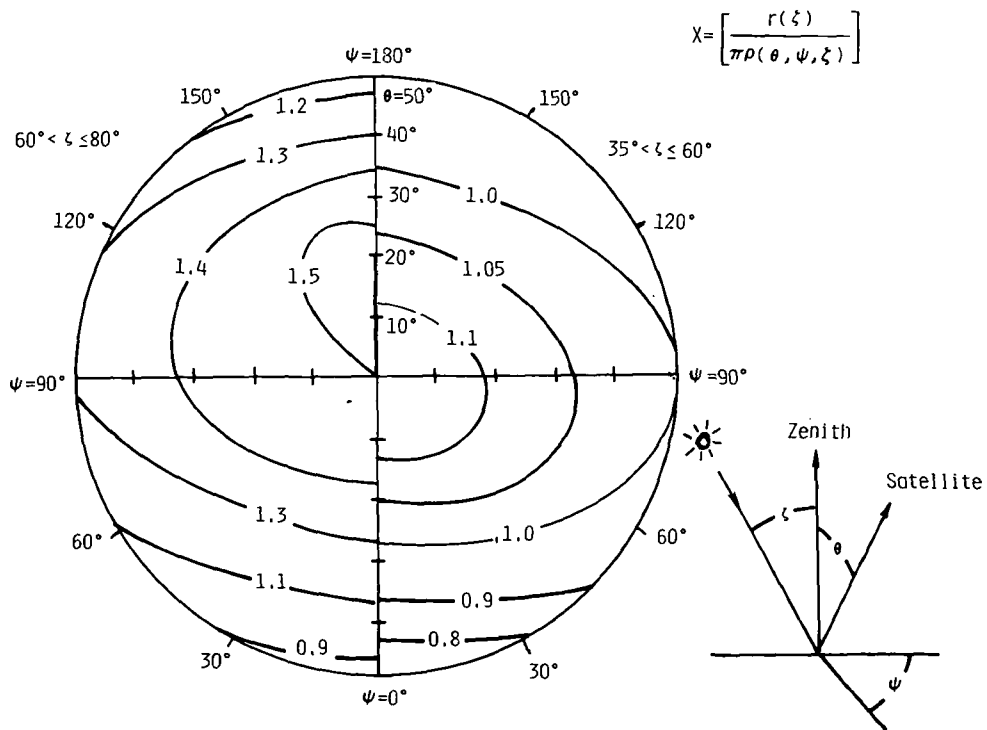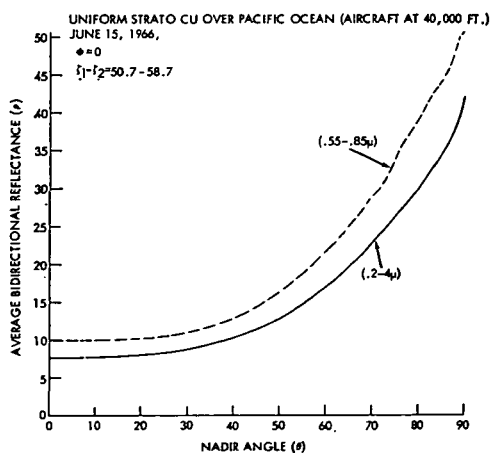

Figure 11.- Shortwave radiation model.
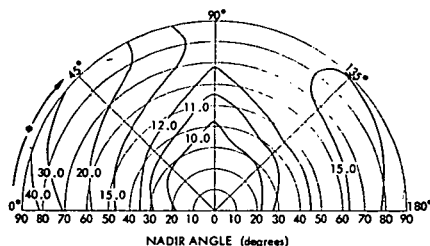
(a) Visible (0.55 to 0.85 μm).

(b) Near-infrared (0.2 to 4.0 μm).

(c) Influence of nadir angle on
bidirectional reflectance.

Figure 12.- Bidirectional reflectances measured by MRIR on
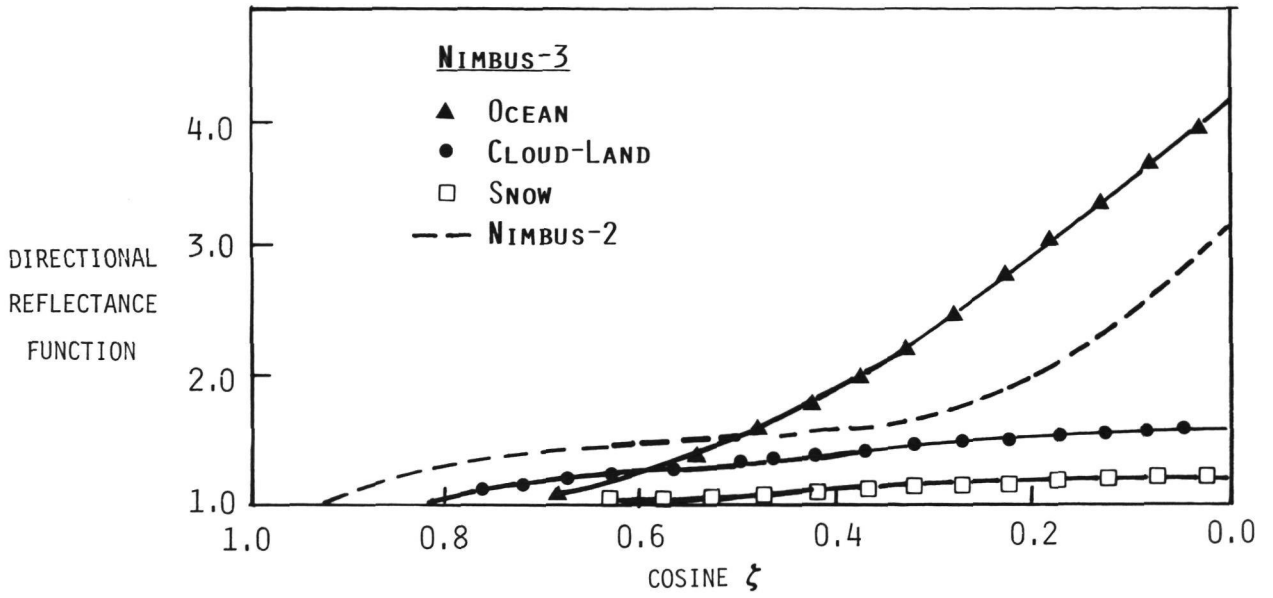NASA Convair 990 (altitude = 40 000 ft).

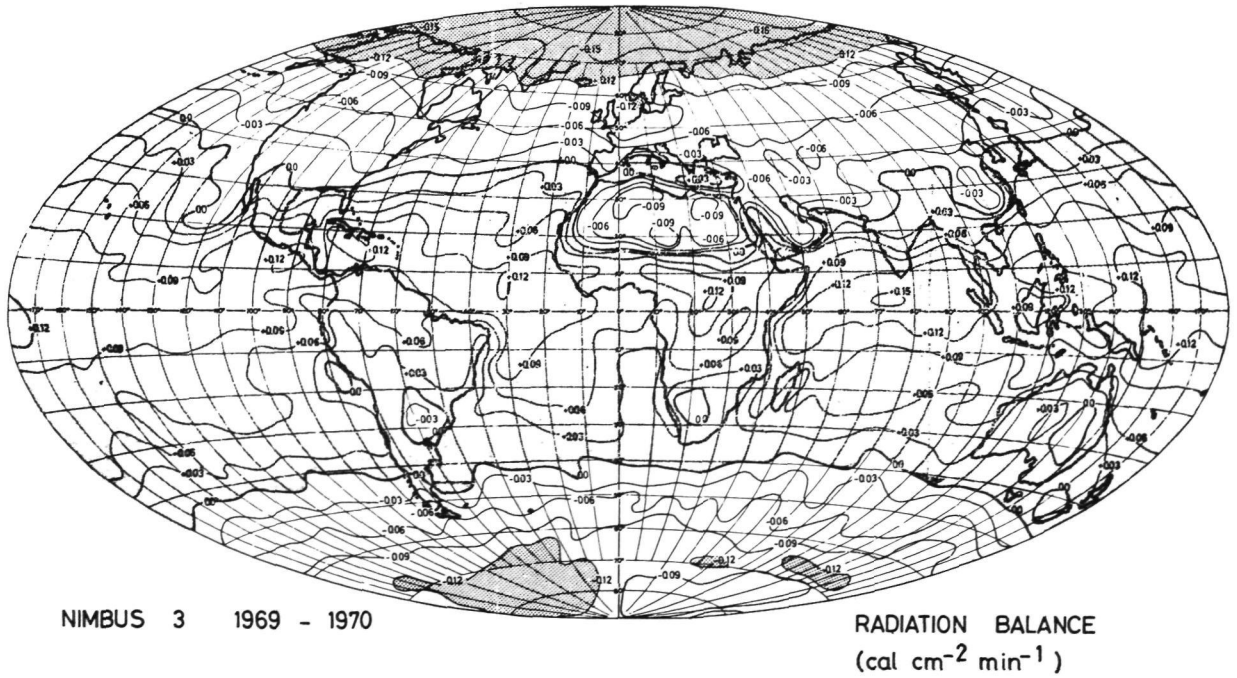Figure 13.- Directional reflectance models used in Nimbus 3 data analysis.

Figure 14.- Global radiation balance as derived from Nimbus 3
measurements. (From Raschke et al., 1973.)

SUN-SYNCHRONOUS
(e.g., NIMBUS, NOAA)

NON-SUN-SYNCHRONOUS
(e.g., TIROS)

Sub-Solar
Longitude

Sub-Solar
Longitude

t + ~1 month

Always passes at
Same Local Time

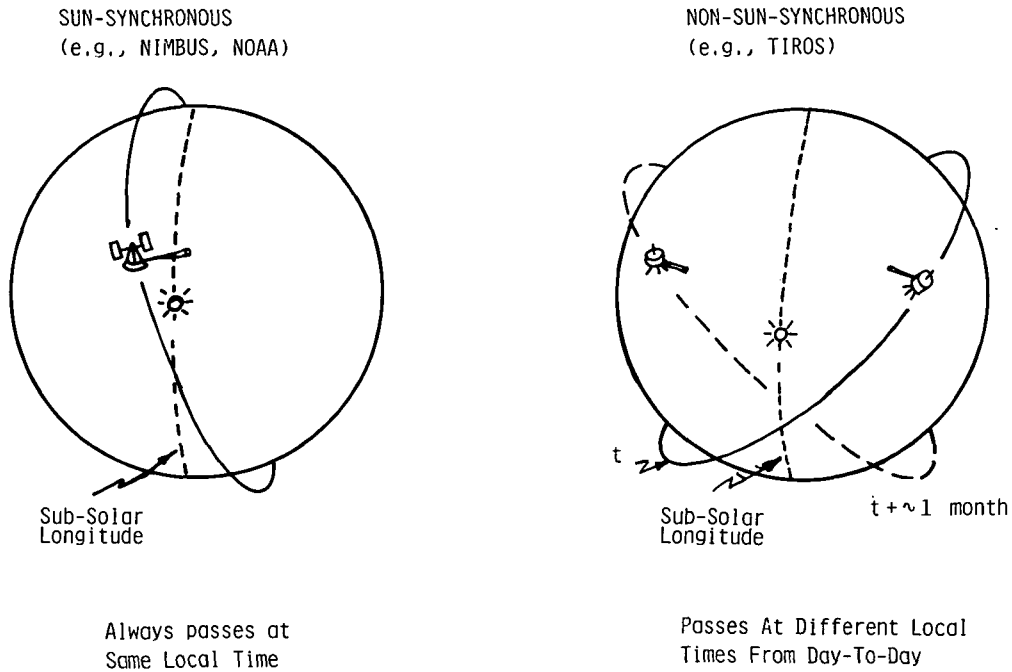Passes At Different Local
Times From Day-To-Day

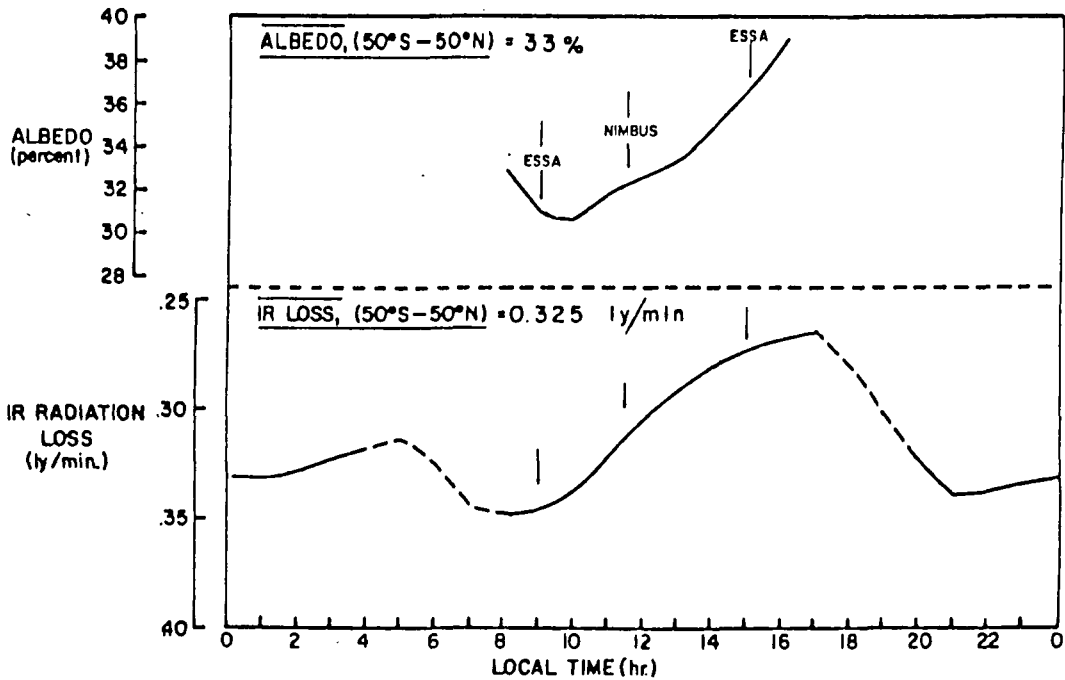Figure 15.- Typical meteorological satellite orbits.

Figure 16.- Diurnal variation of planetary albedo and outgoing
longwave radiation based on TIROS 4 measurements. (From
Vonder Haar, 1968.)